

VIII. PLASMA ELECTRONICS*

Prof. L. D. Smullin	J. R. Cogdell	D. L. Morse
Prof. H. A. Haus	L. J. Donadieu	A. Poeltinger
Prof. A. Bers	B. A. Hartenbaum	S. D. Rothleder
Prof. W. D. Getty	W. C. Homeyer	A. J. Schneider
Prof. D. J. Rose	H. Y. Hsieh	P. E. Serafim
Prof. T. H. Dupree	A. J. Impink, Jr.	P. S. Spangler
Prof. E. P. Gyftopoulos	P. W. Jameson	G. C. Theodoridis
Dr. G. Fiocco	L. E. Lidsky	E. Thompson
W. L. Brassert	P. A. Mandics	J. S. Tulenko
R. J. Briggs		S. Wilensky

A. ELECTRON BEAM-PLASMA INTERACTION EXPERIMENTS

During this quarter, our study has been mainly concerned with observing the nature of the electron beam-plasma interaction in system B.¹ We shall report on the major characteristics of these preliminary observations. The experiments were performed in helium gas. The electron-beam discharge in the helium, as in hydrogen, may be divided into two operating regimes. Regime 1 is characterized by large-amplitude current oscillations of a few tens of megacycles. Regime 2 is characterized by the production of light, x-rays, kilomegacycle rf radiation, and the flow of ion currents to the walls. At low pressures, regime 1 extends throughout the pulse. As the pressure is increased, regime 1 stops after a time, and regime 2 begins. The following observations are concerned with regime 2. Figure VIII-1, which is a schematic drawing of system B, shows the location of our detectors.

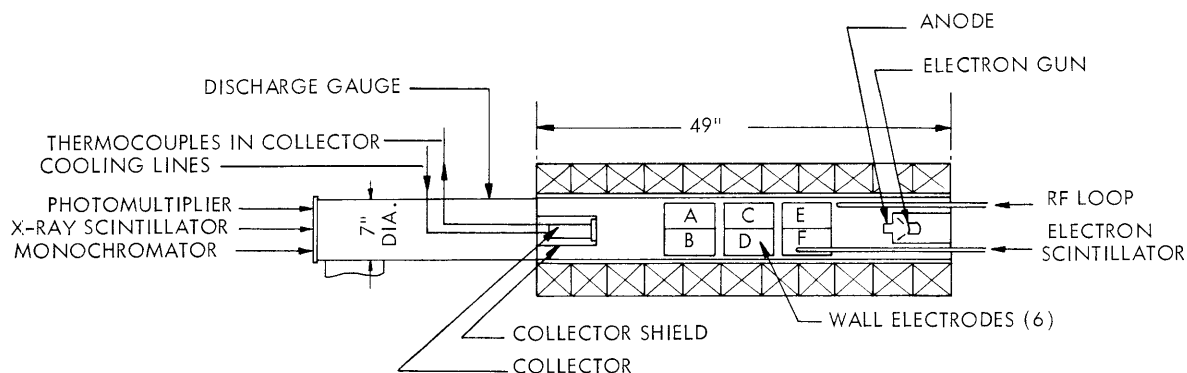


Fig. VIII-1. Location of detectors in system B.

*This work was supported in part by the National Science Foundation (Grant G-24073); in part by the U. S. Navy (Office of Naval Research) under Contract Nonr-1841(78); and in part by Purchase Order DDL B-00368 with Lincoln Laboratory, a center for research operated by Massachusetts Institute of Technology with the joint support of the U. S. Army, Navy, and Air Force under Air Force Contract AF 19(604)-7400.

(VIII. PLASMA ELECTRONICS)

1. Ion Currents

At low pressures, 10^{-4} mm Hg helium, the wall electrodes A-F collect a considerable amount of net ion current. Typically, the average collected ion current is approximately 1 amp, with peak bursts as great as 3 amps, as shown in Figs. VIII-2 and VIII-3. The wall electrodes continue to collect net ion current usually for 100 μ sec after the beam pulse has ended. After this time, a small but long tail of net electron current is observed.

The ion currents are characterized by small amplitude fluctuations that are of the same frequency (50 kc) as the low-frequency fluctuations on the beam collector current, and by large bursts that may or may not repeat. In general, the burstlike nature of the ion currents is more prominent at high magnetic fields. At low magnetic fields, the ion current is usually more steady, with small amplitude fluctuations and occasional bursts.

In Figs. VIII-2 and VIII-3, we observe that the ion current to the top (wall electrodes A, C) are 180° out of phase with the ion current (I_{WD}) to the bottom (wall electrodes B, D). At higher pressures, the net ion currents collected at the wall electrodes decrease. Correspondingly, the anode current collector that collected a net electron current at lower pressures now collects a net ion current, as shown in Fig. VIII-4. This change from predominantly radial ion diffusion to axial ion diffusion, because of change in pressure, is not understood. From a set of oscillograms of currents to the wall electrodes A-F at low pressures, we observe that an average of 46.2×10^{-6} coulombs has flowed to any one of the six wall collectors after the beam pulse has ended. If we assume that the active volume of the plasma is a cylinder, 6 inches in diameter and 36 inches long, and if we assume that there is no ionization after the end of the beam pulse, we obtain an average ion density of 2×10^{11} ions/cc. This estimate of the density might be low because we know that there are electrons near the wall, as shown by the output from an electron scintillator (see Section VIII-D). These electrons are also collected at the wall electrodes as in Fig. VIII-5. The wall electrodes indicate a net ion current that underestimates the total number of ions that are present in the volume. It is also possible that this estimate of the density can be high because the electron scintillator indicates that there are electrons in the volume which are capable of ionization after the pulse has ended. The average ion density of 2×10^{11} ions/cc is approximately a factor of 10 less than the density that we estimate by assuming that the plasma resonance frequency is the 12-15 kmc rf radiation that we observe.

2. Light and Line Broadening

Visually, light seems to emanate uniformly from the cross section of system B. Quantitatively, we have observed that the light produced along the axis and near the wall

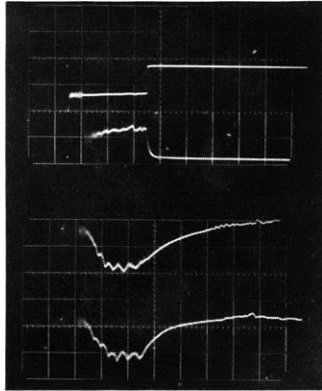


Fig. VIII-2.

I_{cath}
 I_{coll}
 I_{WC}
 I_{WD}

Low-frequency fluctuations on wall currents. Oscillograms of currents are single-sweep displays of a dual-beam Tektronix oscilloscope. (Deflection upward indicates electron collection.) (Beam voltage, 10 kv; induction 324 gauss; pressure, 8×10^{-5} mm Hg; sweep rate, 50 μ sec/cm; current calibrations, $I_{cath} = 1$ amp/cm, $I_{coll} = 1$ amp/cm, $I_{WC} = 0.4$ amp/cm, $I_{WD} = 0.4$ amp/cm.)

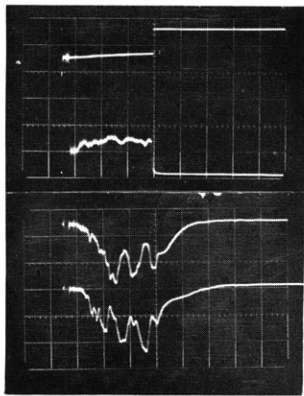


Fig. VIII-3.

I_{cath}
 I_{coll}
 I_{WA}
 I_{WB}

Burstlike wall currents at high magnetic fields. The currents are to wall electrodes near the collector. (Beam voltage, 10 kv; induction, 648 gauss; pressure, 8×10^{-5} mm Hg; current calibrations, $I_{cath} = 1$ amp/cm, $I_{coll} = 1$ amp/cm, $I_{WA} = 1$ amp/cm, $I_{WB} = 1$ amp/cm.)

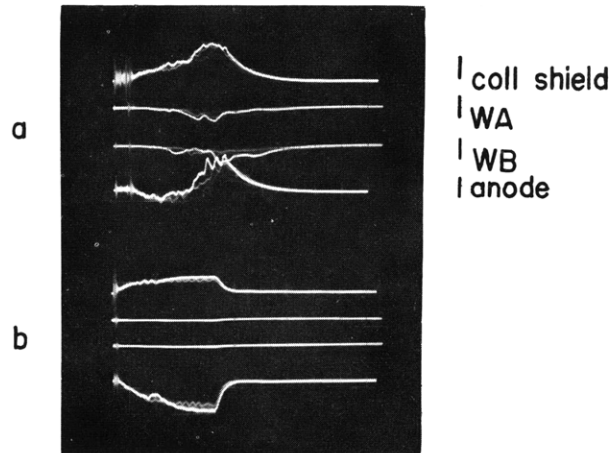


Fig. VIII-4. Currents to various electrodes surrounding plasma as pressure is increased. Note that the anode current represents a net ion flow in (b), while in (a) there is first a net ion flow, followed by a greater net electron flow. (Beam voltage, 12 kv; induction, 540 gauss; (a) pressure, 2×10^{-4} mm Hg; (b) pressure, 4.5×10^{-4} mm Hg; current calibration, 1 amp/cm.)

(VIII. PLASMA ELECTRONICS)

starts at the same time. At pressures of 2×10^{-4} mm Hg there is an afterglow separated from the initial light pulse by a dark interval lasting approximately 100 μ sec, as shown in Fig. VIII-6. The afterglow is more prominent near the walls than along the axis. The dark interval disappears at pressures above 3×10^{-3} mm Hg, as seen in Fig. VIII-6. The width of the helium ion line, 4686 \AA , was measured during the beam pulse and during the afterglow. Two sets of measurements were taken. We used a Jarrel Ash monochromator, 931 A photomultiplier, amplifier, integrator and X-Y recorder to plot the linewidths. The integrator could be adjusted to sample the monochromator output at appropriate times. All results are corrected for instrument

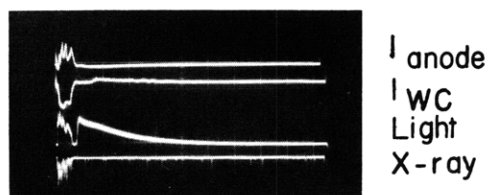


Fig. VIII-5. Dark interval and long afterglow. Afterglow is accompanied by a small fluctuating net electron current to the wall (I_{WC}). (Beam voltage, 10 kv; induction, 296 gauss; pressure, 2×10^{-4} mm Hg; sweep rate, 500 μ sec/cm; $I_{WC} = 0.4$ amp/cm; $I_{anode} = 1$ amp/cm.)

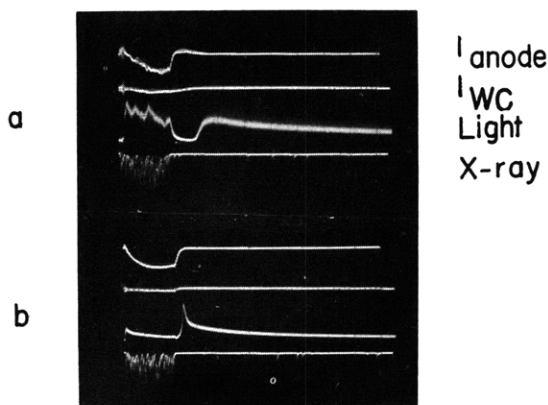


Fig. VIII-6. Light, x-ray, anode current, and wall current for different pressures. The dark interval in light (a) disappears at higher pressure (b). (Beam voltage, 12 kv; induction, 540 gauss; sweep rate, 100 μ sec/cm; (a) pressure, 3×10^{-4} mm Hg; (b) pressure, 3×10^{-3} mm Hg; light calibration, 0.2 v/cm in (a) and 0.5 v/cm in (b).)

broadening.

The first set was taken without a condensing lens and only during the beam pulse. The Doppler broadening at 3×10^{-3} mm Hg pressure, 13.6-kv beam voltage, 10^{-6} perveance, and 540 gauss induction was 0.32 \AA . This corresponds to an ion temperature of 3.1 ev. The second set was taken with a condensing lens. The Doppler broadenings at 7×10^{-4} mm Hg pressure, 10-kv beam voltage, 10^{-6} perveance, and 324 gauss induction were: 0.41 \AA during the beam pulse, and 0.37 \AA in the afterglow. These correspond to ion temperatures of 5.1 ev and 4.2 ev, respectively.

In future experiments, we plan to look at the line broadening along the axis, displaced parallel to the axis, and perpendicular to the axis, with a more systematic variation of parameters and with a more sensitive photomultiplier.

3. Average Power Delivered to the Beam Collector

The change in average power delivered to the beam collector with change in operating conditions was measured calorimetrically. The calorimeter consisted of two series-connected thermocouples placed in the inlet and outlet of the water line that

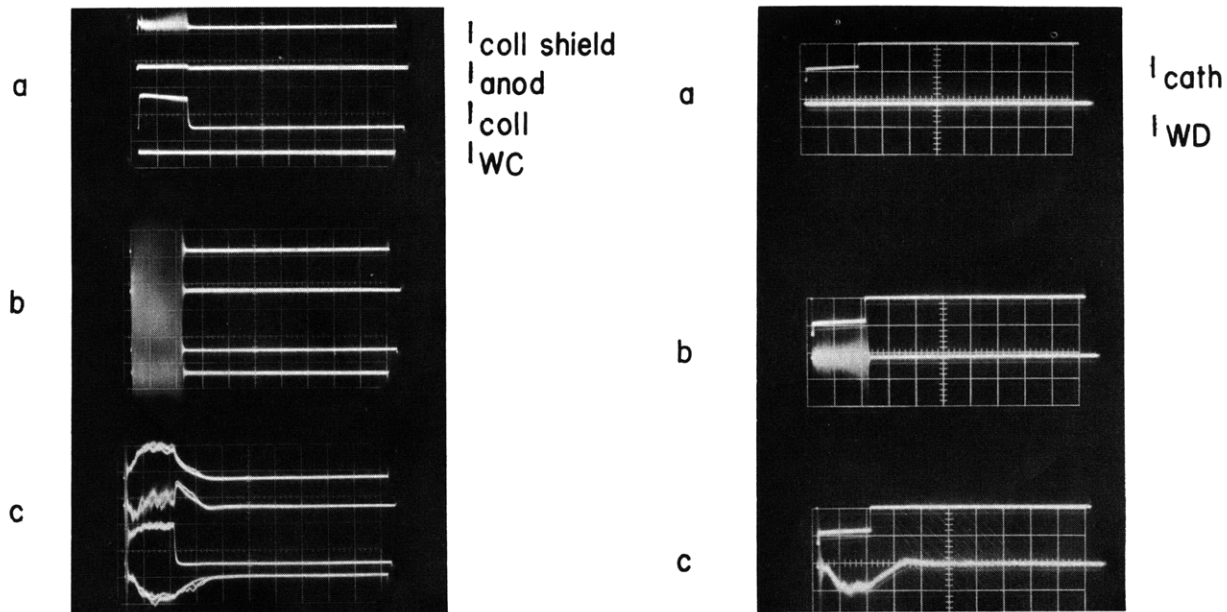


Fig. VIII-7. Electrode currents during calorimetric measurements at different pressures. (a) Pressure = 5×10^{-7} mm Hg. (b) Pressure = 8×10^{-5} mm Hg. (c) Pressure = 2×10^{-4} mm Hg. (Beam voltage, 10 kv; induction, 324 gauss; current calibration, $I_{\text{cath}} = 1$ amp/cm, $I_{\text{coll}} = 0.5$ amp/cm, $I_{\text{WB}} = 0.4$ amp/cm, $I_{\text{WA}} = 0.4$ amp/cm.)

(VIII. PLASMA ELECTRONICS)

cools the beam collector. The net voltage developed across the two thermocouples was measured with a microvoltmeter.

In regime 1, the power delivered to the beam was 11 per cent less than the power delivered under hard vacuum conditions. In regime 2, the power was 30 per cent less than that under hard vacuum conditions. The results are summarized in Table VIII-1. Oscillograms of plasma currents corresponding to the above-mentioned regimes are shown in Fig. VIII-7.

Table VIII-1. Summary of results.

Regime	Pressure (mm Hg)	Beam Voltage (kv)	Induction (gauss)	I_{coll} (amp)	Power (arbitrary units)
hard vacuum	5×10^{-7}	10	324	0.55	10.0
1	8×10^{-5}	10	324	large oscillations	8.9
2	2×10^{-4}	10	324	0.65	7.0

What fraction of the 30 per cent reduction in power goes into plasma heating is not clear. Some of the primary 10-kv electrons may strike the collector shield and not be collected by the collector. The rest of the collector current is attributable to plasma electrons.

We plan to study regime 2 more extensively, as well as to investigate regime 1 and the transition between the two regimes.

L. D. Smullin, B. A. Hartenbaum, H. Y. Hsieh

References

1. L. D. Smullin, W. D. Getty, B. A. Hartenbaum, and H. Y. Hsieh, Electron beam-plasma interaction experiments, Quarterly Progress Report No. 66, Research Laboratory of Electronics, M. I. T., July 15, 1962, pp. 116-123.

B. A STABILITY PROOF FOR MAGNETOHYDRODYNAMIC WAVEGUIDES

In this report we shall demonstrate that a lossless uniform magnetohydrodynamic waveguide of arbitrary dimensions with an axial uniform dc magnetic field is stable. By magnetohydrodynamic waveguide we mean a waveguide containing a beam, also of arbitrary cross section, of compressive fluid flowing parallel to the axis of the waveguide and confined by a discontinuity in the dc magnetic field (see Fig. VIII-8). Since the fluid is assumed to be a perfect conductor and the electric field negligible, the pertinent linearized equations inside the beam are

$$j\omega_r \rho_o \bar{v} = -\nabla_T \left(p + \frac{\bar{B}_o \cdot \bar{B}}{\mu_o} \right) + j\beta \bar{i}_z \left(p + \frac{\bar{B}_o \cdot \bar{B}}{\mu_o} \right) - j\beta \frac{B_o}{\mu_o} \bar{B} \quad (1)$$

$$j\omega_r \bar{B} = -j\beta B_o \bar{v} - \bar{B}_o (\nabla_T \cdot \bar{v}_T - j\beta v_z) \quad (2)$$

$$j\omega_r \rho + \rho_o (\nabla_T \cdot \bar{v}_T - j\beta v_z) = 0 \quad (3)$$

$$p = c_s^2 \rho. \quad (4)$$

Here the symbols have their usual meanings (Eulerian formulation), the electric field and current have been eliminated, and $\omega_r = \omega - v_o \beta$, the frequency in a system moving with beam velocity (v_o).

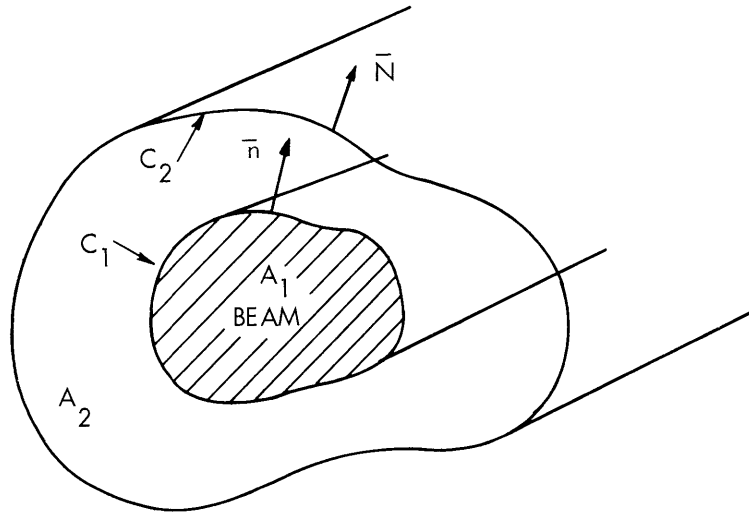


Fig. VIII-8. MHD waveguide.

When the combination

$$j\beta B_o \bar{B}_o \cdot \nabla_T \times (1) - j\omega_r \rho_o \bar{B}_o \cdot \nabla_T \times (2)$$

is made, the following equation results:

$$\left(\omega_r^2 - c_a^2 \beta^2 \right) \bar{B}_o \cdot \nabla_T \times \bar{B}_T = 0, \quad (5)$$

where c_a is the Alfvén speed ($B_o / \sqrt{\mu_o \rho_o}$). Equation 5 shows that two sets of modes can exist in the waveguide. These sets can be distinguished as follows:

(i) One set has a dispersion relation,

$$\beta = \frac{\omega}{v_o \pm c_a},$$

(VIII. PLASMA ELECTRONICS)

and can be shown to have no fields outside the beam. Clearly, these modes are stable.

(ii) The other set of modes is characterized by the vanishing of current (and vorticity) in the axial direction, $\nabla_T \times B_T = 0$, which implies that

$$B_T = \nabla_T \phi, \quad (6)$$

where ϕ is a scalar function of the transverse coordinates. All of the variables in Eqs. 1-4 can be expressed in terms of the scalar potential and its derivatives, provided that it satisfies the equation

$$\nabla_T^2 \phi + k^2 \phi = 0, \quad (7a)$$

where

$$k^2 = \frac{(\omega_r^2 - c_a^2 \beta^2)(\omega_r^2 - c_s^2 \beta^2)}{(c_s^2 + c_a^2) \omega_r^2 - c_s^2 c_a^2 \beta^2}. \quad (7b)$$

Outside the beam, the transverse magnetic field can also be represented as the transverse gradient of a scalar potential, $B_T^0 = \nabla_T \phi^0$, which, with the assumed z -dependence, must satisfy the three-dimensional Laplace equation

$$\nabla_T^2 \phi^0 - \beta^2 \phi^0 = 0. \quad (8)$$

The boundary conditions are too complicated to be examined in detail here (see Cogdell¹), but can be expressed in terms of the scalar potentials quite simply.

On the beam contour:

$$K \bar{n} \cdot \nabla_T \phi = \bar{n} \cdot \nabla_T \phi^0 \quad (9)$$

$$\phi = - \frac{K \beta^2 c_a^2}{\omega_r^2 - c_a^2 \beta^2} \phi^0. \quad (10)$$

On the waveguide wall:

$$\bar{N} \cdot \nabla_T \phi^0 = 0 \quad \sigma = \infty \quad (11)$$

or

$$\phi^0 = 0 \quad \mu = \infty \quad (12)$$

Here, K is the ratio of the time-average magnetic fields outside and inside the beam.

The determinantal equation of the system is determined by dividing Eq. 9 by Eq. 10. The resulting equation must possess real values of ω_r^2 for all real values of β , according to the following line of reasoning. It has been shown,² on the basis of a Lagrangian formulation of the fluid motion, that in the absence of average motion, that is, $v_0 = 0$,

the operator that describes the fluid motion is self-adjoint, which implies that only real values of ω^2 exist for all real values of β . Since ω never occurs in our system equations and boundary conditions except in the combination ω_r , the same must be true there, namely, the determinantal equation can yield only real values of ω_r^2 for all real values of β . If we can prove that ω_r^2 is positive (and thus ω_r real) for all real values of β , then stability is established (see Sturrock³); that is, we have real values of ω for real values of β . We shall now show that for all real values of β no negative values of ω_r^2 can satisfy the equations and boundary conditions.

To establish the result mentioned above, we multiply Eq. 9 by Eq. 10 conjugated and integrate the result around the contour of the beam.

$$K \oint_{C_1} \phi^* (\bar{n} \cdot \nabla_T) \phi ds = \frac{K\beta^2 c_a^2}{\omega_r^2 - c_a^2 \beta^2} \left[\oint_{C_1} \phi^{o*} (-\bar{n} \cdot \nabla_T) \phi^o ds + \oint_{C_2} \phi^{o*} (\bar{n} \cdot \nabla_T) \phi^o ds \right],$$

where the contour integral around C_2 , which vanishes because of Eq. 11 or Eq. 12, has been added for completeness. By Green's theorem the contour integrals can be replaced by area integrals.

$$\int_{A_1} \left[|\nabla_T \phi|^2 + \phi^* \nabla_T^2 \phi \right] da = \frac{\beta^2 c_a^2}{\omega_r^2 - c_a^2 \beta^2} \int_{A_2} \left[|\nabla_T \phi^o|^2 + \phi^{o*} \nabla_T^2 \phi^o \right] da,$$

or, using Eqs. 7 and 8, we have

$$\int_{A_1} \left[|\nabla_T \phi|^2 - k^2 |\phi|^2 \right] da = \frac{\beta^2 c_a^2}{\omega_r^2 - c_a^2 \beta^2} \int_{A_2} \left[|\nabla_T \phi^o|^2 + \beta^2 |\phi^o|^2 \right] da. \quad (13)$$

The left-hand side of Eq. 13 is positive for all negative values of ω_r^2 , since k^2 is negative for negative ω_r^2 , and the right-hand side is negative for all negative ω_r^2 . No solutions, therefore, can exist for negative ω_r^2 and the system is stable. Other forbidden regions in the ω, β plane can be determined through examination of Eq. 13. This result greatly simplifies the numerical solution of the determinantal equation, since only real values of ω must be considered for real β .

J. R. Cogdell

References

1. J. R. Cogdell, A magnetohydrodynamic small-signal power theorem, Quarterly Progress Report No. 66, Research Laboratory of Electronics, M.I.T., July 15, 1962, pp. 123-127.
2. I. B. Bernstein, E. A. Frieman, M. D. Kruskal, and R. M. Kulsrud, An energy principle for hydromagnetic stability problems, Proc. Roy. Soc. (London) A 244, 17-40 (1958).
3. P. A. Sturrock, Kinematics of growing waves, Phys. Rev. 112, 1488-1503 (1958).

(VIII. PLASMA ELECTRONICS)

C. LOW-FREQUENCY TRANSVERSE BEAM-PLASMA INSTABILITY

A number of authors have given analyses of the one-dimensional interaction of a cold electron beam with a cold plasma.^{1, 2} Besides the well-known longitudinal type of interaction that exists with no magnetic field, the presence of a finite magnetic field can result in instabilities associated with waves that are purely transverse. In this report, we show that the gross features of these interactions can be understood by a heuristic use of the theory of weak coupling of modes. The details of the exact analysis of a non-convective low-frequency instability are also summarized.

1. Weak-Coupling Predictions

The system to be analyzed is shown in Fig. VIII-9. We restrict the analysis to the case of waves along the magnetic field and assume a nonrelativistic beam that is relatively weak ($\omega_{pb} \ll \omega_{ce}$, where ω_{pb} is the beam-plasma frequency and ω_{ce} is the electron-cyclotron frequency).

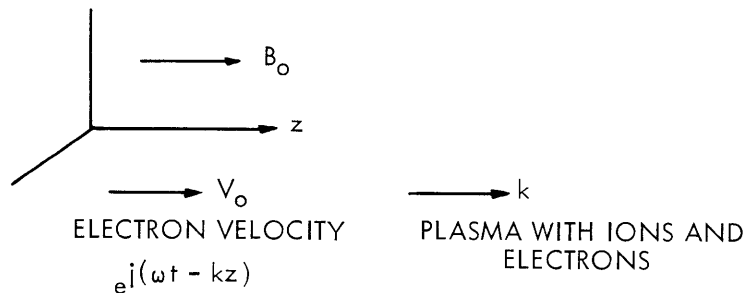


Fig. VIII-9. Beam-plasma system.

The theory of coupling of modes would lead one to expect an instability when an electron-beam wave that carries negative energy is in synchronism with a plasma wave. In Fig. VIII-10, the dispersion diagram for the transverse, left polarized plasma waves is sketched, along with the negative-energy beam waves. (See Section V-A.) From coupling of modes, we would expect a convective instability to occur near ω_{ci} , and a nonconvective instability to occur in the low-frequency regime if $V_0 < U_a$, where U_a is the Alfvén velocity in the plasma. These conclusions are borne out by the exact analysis.^{1, 2}

2. Low-Frequency Nonconvective Instability

The convective instability that is due to the slow cyclotron wave on the beam ($kV_0 \approx \omega + \omega_{ce}$) has been analyzed in some detail.^{1, 2} The low-frequency wave is less

well known, so we shall summarize the results here. The dispersion equation for

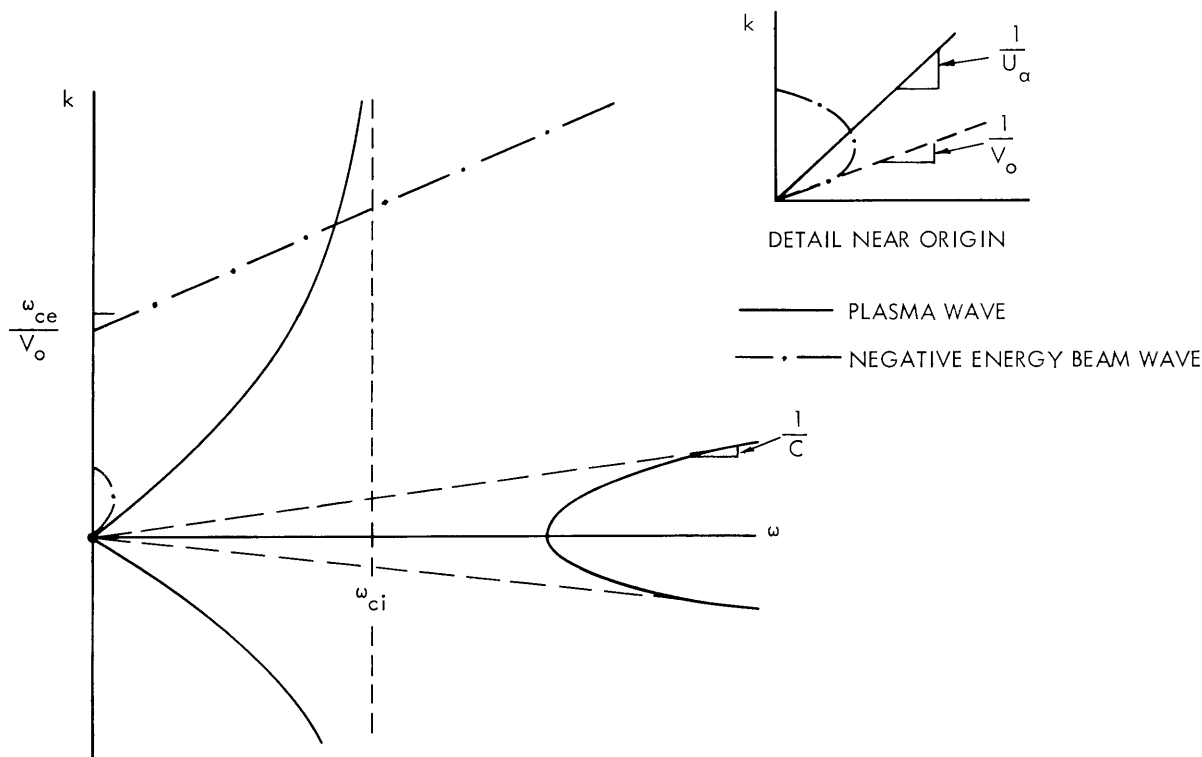


Fig. VIII-10. Superimposed dispersion curves for beam-plasma system.

left polarized waves in a beam-plasma system is

$$\omega^2 - k^2 c^2 - \frac{\omega_{pp}^2 \omega^2}{(\omega - \omega_{ci})(\omega + \omega_{ce})} - \frac{\omega_{pb}^2 (\omega - kV_o)}{(\omega - kV_o + \omega_{ce})} = 0, \quad (1)$$

where ω_{pp} is the plasma's "plasma frequency" and ω_{ci} is the ion-cyclotron frequency. (See Section V-A of this report.) For low frequencies, Eq. 1 becomes

$$\omega^2 - k^2 U_a^2 - \frac{\omega_{pb}^2}{\omega_{pp}^2} \omega_{ci} (\omega - kV_o) = 0, \quad (2)$$

which is a valid expression if $U_a \ll c$ and $\omega_{pb} \ll \omega_{pp}$. For $V_o < U_a$, the resulting dispersion is sketched in Fig. VIII-11a. Since ω is real for all real k , whereas k

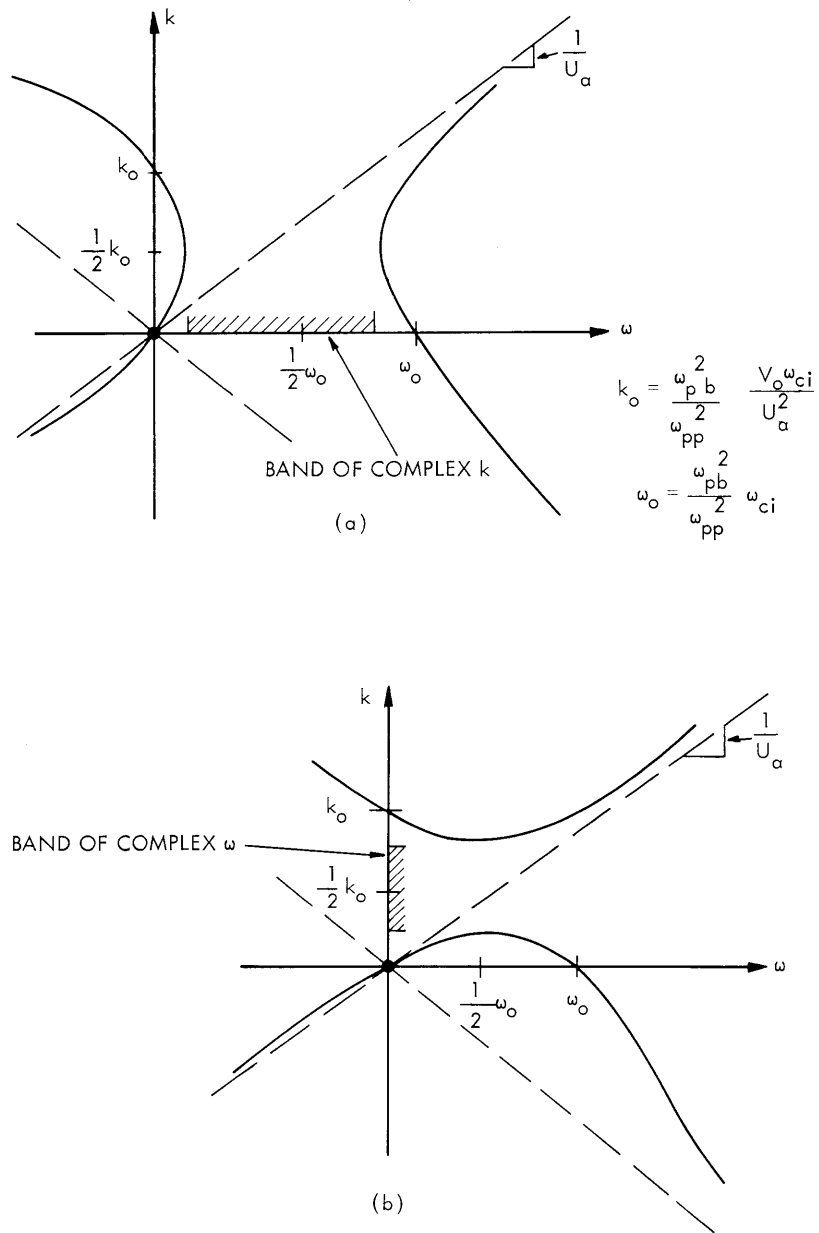


Fig. VIII-11. Low-frequency dispersion: (a) for $V_o < U_a$; (b) for $V_o > U_a$.

is complex for a band of real ω , we have an evanescent wave.³ For $V_o < U_a$, however, the situation is reversed and we now have a nonconvective instability (Fig. VIII-11b).

R. J. Briggs

References

1. See, for instance, M. S. Kovner, Soviet Phys. - JETP 13, 369-374 (1961); N. L. Tointsodze and D. G. Lominidze, Soviet Phys. - Tech. Phys. 6, 759-765 (1961).
2. K. N. Steponov and A. B. Kitsenko, Soviet Phys. - Tech. Phys. 6, 120-126 (1961).
3. P. A. Sturrock, Kinematics of growing waves, Phys. Rev. 112, 1488-1503 (1958).

D. INTERACTION OF A MAGNETOHYDRODYNAMIC FLUID WITH A LUMPED CIRCUIT

The interaction between a perfectly conducting, inviscid fluid flowing with time-average velocity in the presence of a transverse magnetic field and a distributed circuit to which it is coupled has been studied for a number of configurations.¹ Experimental models of magnetohydrodynamic power generators are likely to involve, at most, a few coupling coils, so that an understanding of the interaction not only with distributed circuits, but with lumped circuits as well, is desirable. The present study is illustrative of the latter goal.

We shall calculate the impedance presented at the terminals of two interconnected

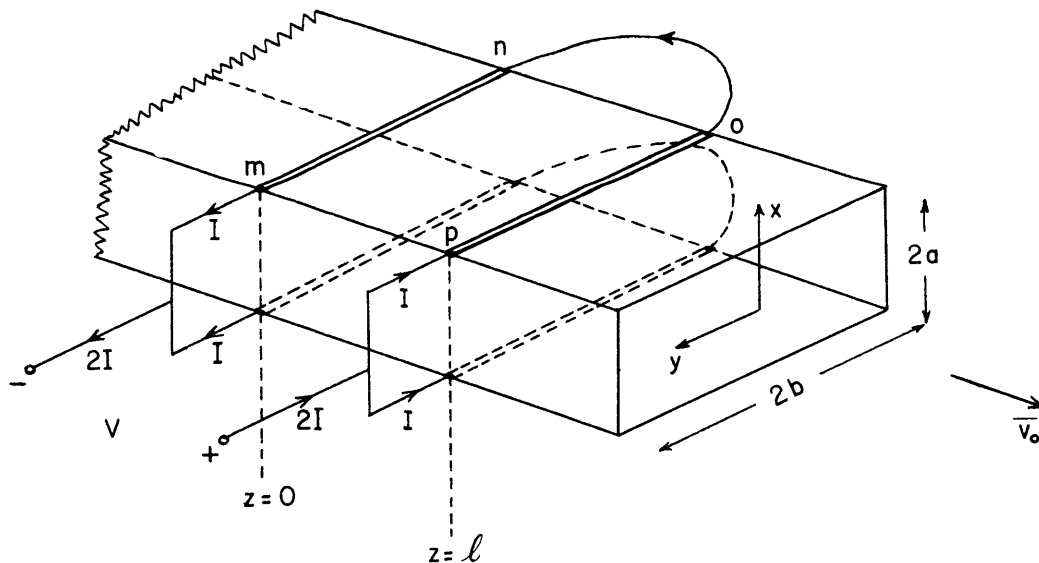


Fig. VIII-12. The rectangular channel and the coupling coils. (The z axis is the longitudinal axis of the channel. The top and bottom yokes have been removed for clarity.)

(VIII. PLASMA ELECTRONICS)

coils that are coupled to a fluid flowing through and completely filling a uniform non-conducting rectangular channel. Nonconducting yokes of infinite permeability are mounted on the top and bottom of the channel and the wires, of negligible thickness, lie between the channel and the yokes. The structure is shown in Fig. VIII-12. The time-average velocity, \bar{v}_0 , is in the z direction and the uniform magnetic field, \bar{B}_0 , is in the x direction. We shall study solutions in which there are x and z components of both the small-signal velocity and magnetic field and y components of the small-signal electric field and current density. The fields are uniform in the y direction.

From previous work¹ we expect the impedance to exhibit a negative real part, at least over some range of frequencies, if v_0 exceeds the magnetoacoustic speed c , where c is the Pythagorean sum of the ordinary sound speed, c_s , and the Alfvén speed, c_b . We restrict the analysis to $v_0 > c$, for which the dispersion relation (Fig. VIII-13) reveals that there are 4 propagating waves for each transverse mode. Each wave has a positive group velocity so that a signal applied to the fluid at $z = 0$ travels only in the positive z direction. The fields in the region between the coils ($0 < z < \ell$) are determined solely by the current I that flows in the wires located at $z = 0$.

The terminal voltage is determined by Faraday's law from the time rate of change of the magnetic flux that spans the contour m-n-o-p shown in Fig. VIII-12. The impedance is given by

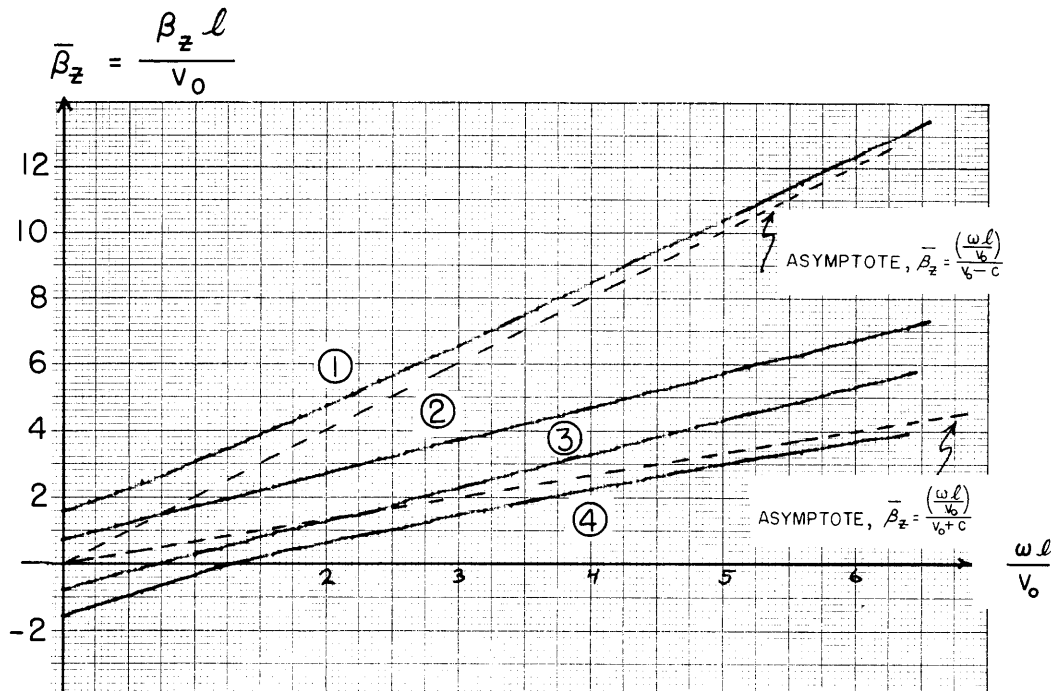


Fig. VIII-13. The dispersion relation.

$$Z = \frac{V}{2I} = j\omega \frac{b}{I} \int_0^{\ell} B_x(a, z) dz. \quad (1)$$

There remains the problem of finding $B_x(a, z)$.

Under the assumption of a time dependence of the form $e^{j\omega t}$, the linearized equations of motion are

$$j\omega \rho_0 \bar{v} + \rho_0 v_0 \frac{\partial \bar{v}}{\partial z} = -\nabla p + \mathbf{J} \times \bar{\mathbf{B}}_0 \quad (2)$$

$$j\omega \rho + v_0 \frac{\partial \rho}{\partial z} = -\rho_0 \nabla \cdot \bar{v} \quad (3)$$

$$\bar{\mathbf{E}} + (\bar{v}_0 \times \bar{\mathbf{B}}) + (\bar{v} \times \bar{\mathbf{B}}_0) = 0 \quad (4)$$

$$\nabla \times \bar{\mathbf{E}} = -j\omega \bar{\mathbf{B}} \quad (5)$$

$$\nabla \times \frac{\bar{\mathbf{B}}}{\mu_0} = \bar{\mathbf{J}} \quad (6)$$

$$p = c_s^2 \rho \quad (7)$$

The time-average mass density is denoted by ρ_0 and the small-signal variables appear without subscripts. Form the expression

$$\bar{v} \cdot (\text{Eq. 2})^* + \frac{p}{\rho_0} (\text{Eq. 3}) - \bar{\mathbf{J}}^* \cdot (\text{Eq. 4}) + \bar{\mathbf{H}}^* \cdot (\text{Eq. 5}) - \bar{\mathbf{E}} \cdot (\text{Eq. 6})^*. \quad (8)$$

With some rearrangement, the real part of Eq. 8 is

$$\text{Re } \nabla \cdot (\bar{\mathbf{E}} \times \bar{\mathbf{H}}^* + p^* \bar{v}) + \frac{\partial}{\partial z} \left(\frac{\rho_0 v_0 |\bar{v}|^2}{2} + \frac{v_0 p^* \rho}{2\rho_0} \right) + \bar{v}_0 \cdot \text{Re } (\bar{\mathbf{J}}^* \times \bar{\mathbf{B}}) = 0. \quad (9)$$

Equation 9 would be a small-signal power theorem if it were not for the last term. All attempts to rewrite this term in terms of a divergence and/or z derivative have failed, thus far. The term is reminiscent of one involving the curl of the generalized momentum which appears in an analogous relation that is pertinent to an electron beam.² For the present purpose of obtaining a conservation theorem we use Eq. 6 to transform the last term of Eq. 9 into

$$\bar{v}_0 \cdot \left\{ \text{Re} \left(\frac{\bar{\mathbf{B}} \cdot \nabla \bar{\mathbf{B}}^*}{\mu_0} \right) - \nabla \left(\frac{\bar{\mathbf{B}} \cdot \bar{\mathbf{B}}^*}{2\mu_0} \right) \right\}.$$

The transformed equation is then integrated over the volume of the channel that is included between two transverse planes located an arbitrary distance apart. The result, after introducing the appropriate components and using the boundary conditions, is the

(VIII. PLASMA ELECTRONICS)

conservation relation

$$\frac{\partial}{\partial z} \iint_{\text{cross section}} \left\{ \text{Re} \left(\frac{-E_y B_x^*}{2\mu_0} + \frac{p^* v_z}{2} \right) + v_0 \left(\frac{|B_z|^2}{4\mu_0} - \frac{|B_x|^2}{4\mu_0} + \frac{\rho_0 |v_x|^2}{4} + \frac{\rho_0 |v_z|^2}{4} + \frac{p^* \rho}{4\rho_0} \right) \right\} d\sigma = 0. \quad (10)$$

It has been shown² that such a conservation theorem provides the basis for an orthogonality relation between two waves of unlike (imaginary) propagation constant.

We expand the fields of a single wave in terms of the transverse modes. For example,

$$B_x(x, z) = \sum_{n=0}^{\infty} a_n \hat{B}_x^{(n)}(x) \exp[-j\beta_z^{(n)} z]. \quad (11)$$

For the problem under consideration we need only the solution for which v_z is symmetric in x .

$$\hat{V}_x^{(n)}(x) = A \sin \beta_x x \quad (12a)$$

$$\hat{V}_z^{(n)}(x) = \frac{jAY}{\beta_x \beta_z c_s^2} \cos \beta_x x \quad (12b)$$

$$\hat{B}_x^{(n)}(x) = \frac{jAB_0 Y}{\omega_r \beta_x c_s^2} \cos \beta_x x \quad (12c)$$

$$\hat{B}_z^{(n)}(x) = \frac{-AB_0 Y}{\omega_r \beta_z c_s^2} \sin \beta_x x \quad (12d)$$

$$\hat{\rho}^{(n)}(x) = \frac{jA\rho_0 \omega_r}{\beta_x c_s^2} \cos \beta_x x \quad (12e)$$

$$\hat{E}_y^{(n)}(x) = \frac{-jA\omega B_0 Y}{\omega_r \beta_x \beta_z c_s^2} \cos \beta_x x \quad (12f)$$

Here, A is a complex amplitude, $\omega_r = \omega - v_0 \beta_z$, $Y = \omega_r^2 - c_s^2 \beta_x^2$ and $\beta_x = \frac{n\pi}{a}$ ($n=0, 1, 2, 3, \dots$).

The discontinuities in the fields which are caused by a transverse current sheet source, $K_d(x)$ (for the two wires at $z = 0$ carrying the current I , $K_d(x) = I\{\delta(x-a) + \delta(x+a)\}$) are found as follows. We introduce into Eq. 6 a source current density, $J_d(x, z) = K_d(x) \delta(z)$ and integrate Eqs. 2-6 with respect to z from $z = 0^-$ to $z = 0^+$. The quantities v_x , B_z , and E_y are found to be continuous across the sheet, while the discontinuities in the other quantities are given by

$$\Delta v_z = \frac{B_o v_o}{\rho_o (v_o^2 - c^2)} K_d(x) \quad (13a)$$

$$\Delta B_x = \frac{-B_o^2}{\rho_o (v_o^2 - c^2)} K_d(x) \quad (13b)$$

$$\Delta \rho = \frac{-B_o}{(v_o^2 - c^2)} K_d(x). \quad (13c)$$

Because no excitation can propagate upstream, all small-signal quantities are zero at $z = 0^-$ and Eqs. 13 give the fields themselves at $z = 0^+$. With these fields known, the coefficients a_n can be determined from the orthogonality condition.

$$a_n = \frac{j(-1)^{n+1} B_o I \omega_r^2 \beta_x \beta_z c_s^2 Y}{a \rho_o A D}, \quad (14)$$

where

$$D = \omega_r^2 \beta_z^2 c_s^2 v_o \left(\omega_r^2 + c_s^2 \beta_x^2 \right) + 2Y \omega_r^3 \beta_z c_s^2 + Y^2 \left\{ 2\omega \beta_z c_b^2 + \omega_r^2 v_o + v_o c_b^2 (\beta_x^2 - \beta_z^2) \right\}.$$

For a single wave $B_x(x, z)$ is obtained by combining Eqs. 11, 12c, and 14. The impedance itself is obtained from Eq. 1. Superposing all four waves, enumerated by the letter ν , we finally have

$$Z(\omega) = \mu_o \frac{c_b^2}{c} \frac{b}{a} \sum_{\nu=1}^4 \sum_{n=0}^{\infty} \left(e^{-j\beta_z \ell} - 1 \right) F, \quad (15)$$

where the weighting function F is given by

$$F = -c \omega \omega_r \frac{Y^2}{D}. \quad (16)$$

Although not indicated explicitly in Eqs. 15 and 16, both β_z and F are functions of ν , n , and ω .

Figure VIII-14 shows F plotted against the dimensionless quantity $\frac{\omega \ell}{v_o}$ for the next to lowest order mode ($n=1$) for $v_o = 2c = 4c_s = \frac{4}{\sqrt{3}} c_b$. Both (β_z/n) and F can be shown to be functions of the ratio ω/n , so that Figs. VIII-13 and VIII-14 are representative of any mode ($n \neq 0$). In Figs. VIII-13 and VIII-14 like-numbered branches pertain to the same wave. Notice from Fig. VIII-14 that two of the waves are dominant, namely, those corresponding to branches 1 and 4 for which the dispersion relation is asymptotic to the lines $\bar{\beta}_z = \frac{\omega \ell / v_o}{v_o \pm c}$ for large ω . Indeed, these correspond to the fast and slow waves that

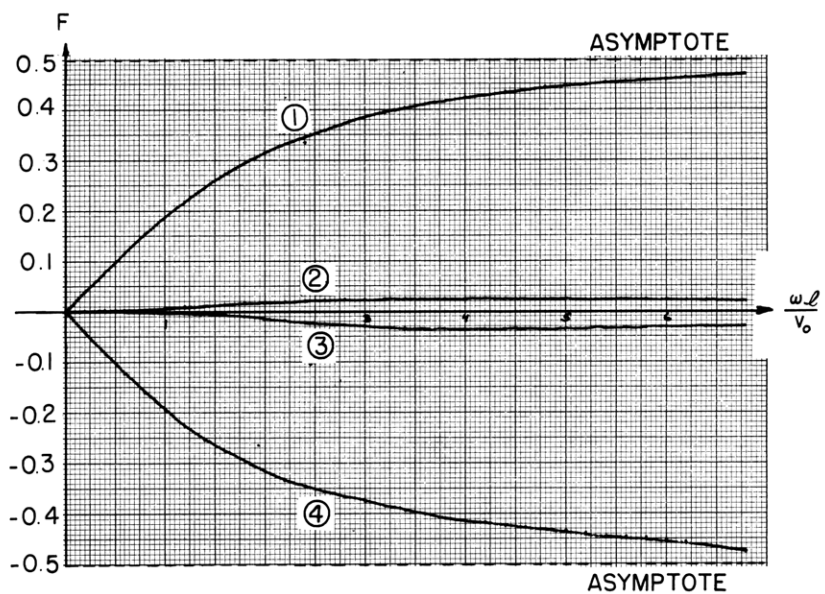


Fig. VIII-14. The weighting function.

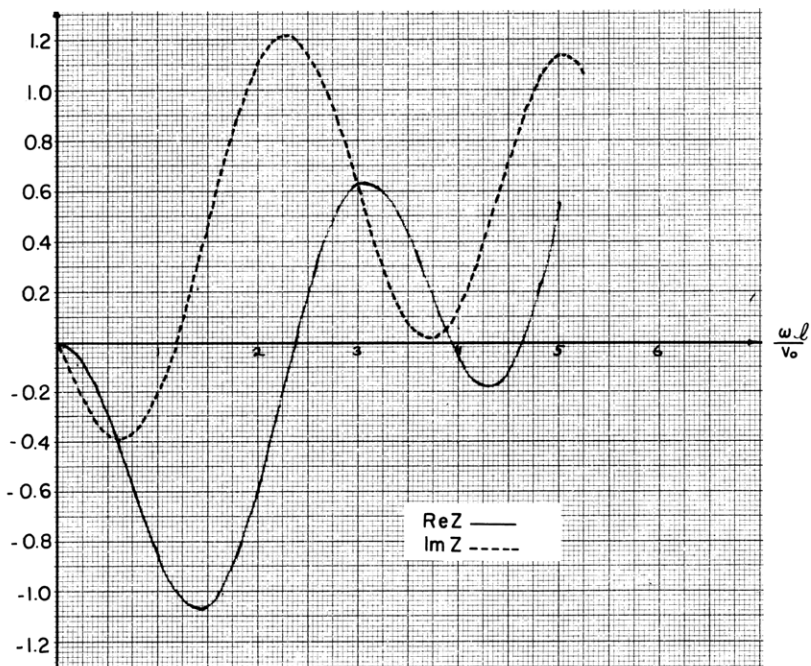


Fig. VIII-15. The resistive and reactive components of the impedance presented at the coil terminals.

are found in a one-dimensional model of a perfectly conducting fluid.¹

Figure VIII-15 shows the real and imaginary parts of the impedance as a function of $\frac{\omega l}{v_0}$. Eight transverse modes were used in the calculations.

The calculations for Figs. VIII-13, VIII-14 and VIII-15 were performed on the IBM 7090 digital computer of the Computation Center, M. I. T.

A. J. Schneider

References

1. H. A. Haus, Alternating-current generation with moving conducting fluids, *J. Appl. Phys.* 33, 2161 (1962).
2. D. L. Bobroff and H. A. Haus, Uniqueness and Orthogonality of Small-Signal Solutions in Electron Beams, Technical Report No. 31, Raytheon Manufacturing Company, Waltham, Massachusetts, June 10, 1958.

E. SCINTILLATING PROBE FOR PLASMAS

We have built a scintillating probe to estimate the density and energy of the electrons in a plasma. The scintillating material is located at the end of a light pipe, and is inserted in the vacuum system through a sliding seal. The light pipe terminates at the face of a photomultiplier, whose output is displayed and analyzed. At present, we are experimenting with plastic probes in the form of small cylinders; the diameter of the probe is 5 mm; the length outside the shield is 10 mm but we plan to use smaller configurations. The probe is coated with an Al film to prevent light from entering the photo-detector; the film has a thickness of 2 μ , which is approximately the range of electrons at 20 kev. Thus the film renders the scintillator insensitive to low-energy particles. By using a small-volume scintillator, one expects to reduce the probability of detecting X-rays in order to make the probe essentially sensitive to energetic electrons. Further discrimination will be achieved by the insertion of a removable screen and also by observing the spatial distribution of the illumination of the scintillator.

G. Fiocco

F. PRODUCTION OF ION BEAMS

The experiment described in Quarterly Progress Report No. 66 (pages 137-139) has been operated. Currents of 13 ma at voltages of 30 kv were obtained with divergences of the order of 1.5°. The current appears to have been limited by breakdown over the surface of the lens insulator, but this has not yet been remedied as most of our time has been spent in the assembly of the Thomson scattering experiment described in Section VIII-G.

We hope to also use the laser to demonstrate the breakup of molecular ions which

(VIII. PLASMA ELECTRONS)

was predicted by Hiskes¹ and observed under dc conditions by Riviere and Sweetman² and others.

If we can focus the approximately 100-kw pulse of coherent radiation from the laser into a 0.1-mm diameter beam, we should obtain fields of the order of 3.5×10^7 volts per meter. Larger fields than this can be obtained, however, as it is suspected that the laser output is in a series of larger spikes, the peak amplitude of which may exceed 100 kw.

Preliminary calculations show that starting with 10 ma of H_2^+ ions in a 1-cm diameter beam, we should detect 2.5 μ a of protons per pulse if we assume 1 per cent beam breakup.

This figure is obtained by assuming only one traversal of the laser beam by the ion beam corresponding to a time in the field of 5×10^{-11} sec. Hiskes has shown that breakup of the highly excited states will occur in 10^{-18} sec but because of tunnelling effect, the probability of breakup increases quite markedly as the time spent in the field is increased.

We could achieve this effect by reflecting the laser beam through the ion beam several times by using mirrors.

The design of the spectrometer for beam analysis is almost complete, and the laser components have been assembled and operated in preparation for the Thomson scattering experiment.

E. Thompson, G. Fiocco

References

1. J. R. Hiskes, Phys. Rev. 122, 1207 (1961).
2. A. C. Riviere and D. R. Sweetman, Phys. Rev. Letters 5, 560 (1960).

G. SCATTERING OF LIGHT FROM ELECTRONS

In order to establish the feasibility of using a laser beam as a diagnostic tool for plasmas, we have prepared some preliminary experiments to observe Thomson scattering from an electron beam. By observing the scattered radiation at a suitable angle with respect to the electron beam, one obtains signals that are characterized by large Doppler shifts. These are easier to detect against the low background illumination than a distribution that is spread out and centered about the transmitted frequency, as would be the case for a stationary and luminous plasma.

The experimental apparatus consists of a vacuum chamber in which a ruby laser beam intersects an electron beam at normal incidence. The region of intersection is observed through an optical system, which includes a photodetector, whose optical axis

makes a fixed angle with the axis normal to the plane containing the beams. The observing system, however, can be rotated around that normal axis to allow observation at a variety of angles; therefore different values for the Doppler shift can be obtained. At present, we are utilizing an interference filter to obtain the spectral resolution and we plan to use a grating monochromator. A 50-joule laser beam, at $\lambda \approx 6934 \text{ \AA}$, and an electron beam of 100 ma at 2 kv are being used.

G. Fiocco, E. Thompson

H. USE OF FISSILE NUCLIDES IN FUSION REACTOR BLANKETS

A study has been initiated to explore the feasibility and merits of including fissile nuclides in a fusion reactor blanket. The fissile nuclides of primary interest are thorium 232 and uranium 238, both of which are available in relatively large quantities and at rather lower cost than the thermally fissionable isotopes.

The expected advantages of including these fissile nuclides in a blanket are (a) an increase in the power output of the system by virtue of the high-energy fissions induced; (b) breeding of fissionable nuclides by neutron capture in either thorium or uranium; and (c) improvement of the neutron economy of the system because of the high neutron yield of high-energy fissions.

Anticipated difficulties are (a) a possible increase in the severity of the corrosion problem if the fissile nuclides are introduced into the fused salts; (b) severe radiation damage if the fissile nuclides are in solid form, as in the first wall; and (c) an appreciable increase in the radiation levels encountered because of the high activity of fission products with attendant difficulties in radioactive-waste disposal.

At this time, the investigation has been concentrated on the problem of neutron economy and tritium regeneration. Scattering matrices for uranium 238 and thorium 232 have been developed, and preliminary calculations of neutron flux and neutron-induced reaction rate distributions have been made by using digital computer codes.^{1,2} As an adjunct to the study, the method of calculating multigroup equivalent resonance absorption cross sections has been extended to include those cases in which the absorbing nuclide is present as a constituent of a homogeneous mixture.

Two different configurations are under consideration. In one, the fissile nuclide is present in metallic form in the first wall; in the other, it is included as a component of the first-wall coolant. Since thorium may be structurally feasible for first-wall applications because of its refractory characteristics, neutronic calculations were made for a thorium first wall, 2 cm thick. The calculated tritium breeding ratio was 1.05, insufficient (even if the leakage were fully recovered) to support a self-sustaining tritium breeding cycle. For purposes of comparison, a run was made for a uranium 238 first wall, 1.5 cm thick, which is equivalent in total nuclide population to 2 cm of thorium. The result was a tritium breeding ratio of 1.41. The improvement in neutron economy

(VIII. PLASMA ELECTRONICS)

is attributed in part to the higher fission cross section and fission neutron yield of uranium at 14 mev, and in part to the lower resonance absorption of uranium compared with thorium. Because of the low melting point of uranium metal, there appears to be little hope of exploiting its better neutronic characteristics, as least in solid form. The results and the pertinent data for these two calculations are compared in Table VIII-2.

Table VIII-2. Results of calculations.

First Wall		
Composition	Th ²³²	U ²³⁸
Thickness	2.00 cm	1.50
Results		
Fission rate	0.034	0.169
First-wall multiplication	0.240	0.721
First-wall absorption	0.219	0.344
Total neutron leakage	0.058	0.059
Tritium regeneration ratio	1.050	1.410

In both cases the first-wall coolant region was 6.25 cm thick and contained 66 LiF-34BeF₂. The attenuator region was 56 cm thick and contained 79 per cent (66LiF-34BeF₂) and 21 per cent graphite.

All compositions are given in mole fraction percentages.
All results are per unit primary source neutron.

Preliminary calculations have also been made for LiF-BeF₂-UF₄ fused salts in the first-wall coolant region. Introduction of the fissile nuclide into the fused-salt coolant offers the important advantage that the high-energy densities associated with fission occur in the coolant and alleviate the problem of heat transfer, for example, from the first wall. The fused-salt system that was chosen seems to be the only suitable one, since all others that were examined have prohibitively high melting points. Thorium-fused salts offer no advantages over uranium systems because of the lower fission rate and higher neutron absorption associated with thorium, and therefore we did not study them. From the point of view of materials, the upper limits for the melting point and viscosity of practical first-wall coolants appear to be ~ 500°C and 10 centipoises, respectively.

(VIII. PLASMA ELECTRONICS)

At present, four fused-salt calculations have been completed. The two salts of particular interest are the $73\text{LiF}-27\text{UF}_4$ system and the $60\text{LiF}-30\text{BeF}_2-10\text{UF}_4$ mix, where the numbers indicate mole percentages. Both melt at $\sim 500^\circ\text{C}$. The first salt contains the maximum concentration of uranium atoms which is attainable at the limiting melting point. The second optimizes the beryllium content for a 10 mole per cent UF_4 mixture. For each system calculations were made for a 2.5-cm and a 1.0-cm molybdenum first wall to observe the effects of varying the high-energy neutron population in the fused-salt region. The results and corresponding data are listed in Table VIII-3.

Table VIII-3. Experimental results.

First Wall				
Composition	Mo	Mo	Mo	Mo
Thickness	2.50 cm	1.00 cm	2.50 cm	1.00 cm
Coolant				
Composition ($\text{LiF}-\text{BeF}_2-\text{UF}_4$)	73-00-27	73-00-27	60-30-10	60-30-10
Thickness	6.68 cm	6.68 cm	6.25 cm	6.25 cm
Results				
Fission rate	0.051	0.066	0.021	0.027
Uranium 238 multiplication	0.222	0.291	0.092	0.120
Uranium 238 absorption	0.246	0.231	0.111	0.101
Total neutron leakage	0.076	0.088	0.079	0.093
Tritium regeneration ratio ^a	1.050	1.070	1.080	1.070
In both cases the attenuator region was 49 cm thick and contained 79 per cent ($66\text{LiF}-34\text{BeF}_2$) and 21 per cent graphite.				
All compositions are given in mole percentages.				
All results are given per unit primary source neutron.				
a. It should be noted that a 20-cm increase in the thickness of the third region would yield a gain of approximately 0.05 in tritium breeding ratios by recovering neutrons counted as leakage here.				

The potential increase in the power output of the thermonuclear device where high-energy fission in uranium 238 or thorium 232 is exploited is illustrated by the first case

(VIII. PLASMA ELECTRONICS)

in Table VIII-3. Since a fission event yields nearly 10 times as much energy as a D-T fusion, a fission rate of 0.05 represents an increase in thermal-power output of 50 per cent. Also, in a conventional thermal fission reactor, complete utilization of the 0.25 plutonium atoms generated per fusion represents a potential increase in power of approximately 250 per cent. Thus in an optimized case the total thermal-power output of a fusion-fission complex fueled with deuterium, lithium, and uranium 238 may be approximately 300 per cent of that obtained by fusion alone.

Since the fused-salt coolant will necessarily be processed to recover tritium, simultaneous recovery of plutonium and removal of fission products should present neither insuperable problems nor a great increase in cost.

Calculations will be made for several other fused salts with varying uranium content. Codes^{1,2} will be used to determine the heating rates in the blanket for all cases under investigation. The maximum possible rate of heat removal may well be the determining factor in setting the upper limit for the fissile nuclide concentration in the blanket assembly.

L. N. Lontai, A. J. Impink, Jr.

References

1. W. G. Homeyer and A. J. Impink, Energy extraction blanket for a fusion reactor, Quarterly Progress Report No. 64, Research Laboratory of Electronics, M.I.T., January 15, 1962, pp. 128-131.
2. W. G. Homeyer, A. J. Impink, and D. J. Rose, Energy extraction blanket for a fusion reactor, Quarterly Progress Report No. 66, Research Laboratory of Electronics, M.I.T., July 15, 1962, pp. 142-150.